The Astrophysical Journal, 967:15 (10pp), 2024 May 20 https://doi.org/10.3847/1538-4357/ad3e7b

Infall Motions in the Hot Core Associated with the Hypercompact H II Region G345.0061 +01.794 B

Toktarkhan Komesh[1,2], Guido Garay[3], Christian Henkel[4,5,6], Aruzhan Omar[2,7], Robert Estalella[8], Zhandos Assembay[2,7], Dalei Li[5], Andrés Guzmán[9], Jarken Esimbek[5], Jiasheng Huang[10], Yuxin He[5], Nazgul Alimgazinova[1,2,7], Meiramgul Kyzgarina[1,2,7], Shukirgaliyev Bekdaulet[1,11,12,13], Nurman Zhumabay[1,2,14], and Arailym Manapbayeva[2,7]
[1] Energetic Cosmos Laboratory, Nazarbayev University, Astana 010000, Kazakhstan; toktarkhan.komesh@nu.edu.kz, guido@das.uchile.cl
[2] Institute of Experimental and Theoretical Physics, Al-Farabi Kazakh National University, Almaty 050040, Kazakhstan
[3] Departamento de Astronomia, Universidad de Chile, Camino el Observatorio 1515, Las Condes, Santiago, Chile
[4] Max-Planck-Institut für Radioastronomie, Auf dem Hügel 69, 53121 Bonn, Germany
[5] Xinjiang Astronomical Observatory, Chinese Academy of Sciences, Urumqi 830011, People's Republic of China
[6] Astronomy Department, King Abdulaziz University, PO Box 80203, Jeddah 21589, Saudi Arabia
[7] Faculty of Physics and Technology, Al-Farabi Kazakh National University, Almaty 050040, Kazakhstan
[8] Departament de Física Quàntica i Astrofísica, Institut de Ciències del Cosmos, Universitat de Barcelona, IEEC-UB, Martí i Franquès 1, 08028 Barcelona, Spain
[9] National Astronomical Observatory of Japan, National Institutes of Natural Sciences, 2-21-1 Osawa, Mitaka, Tokyo 181-8588, Japan
[10] Chinese Academy of Sciences South America Center for Astronomy, National Astronomical Observatories, Chinese Academy of Sciences, Beijing 100101, People's Republic of China
[11] Heriot-Watt International Faculty, Zhubanov University, 263 Zhubanov Brothers Street, 030000 Aktobe, Kazakhstan
[12] Department of Computation and Data Science, Astana IT University, 55/11 Mangilik El Avenue, 010000 Astana, Kazakhstan
[13] Fesenkov Astrophysical Institute, 23 Observatory Street, 050020 Almaty, Kazakhstan
[14] Institute of Mathematics, Physics and Informatics, Abai Kazakh National Pedagogical University, Almaty 050010, Kazakhstan
Received 2024 February 8; revised 2024 April 13; accepted 2024 April 13; published 2024 May 13

Abstract

We report high angular resolution observations, made with the Atacama Large Millimeter Array in band 6, of high excitation molecular lines of CH_3CN and SO_2 and of the H29α radio recombination line toward the G345.0061 +01.794 B HC H II region in order to investigate the physical and kinematical characteristics of its surroundings. Emission was detected in all observed components of the $J = 14 \rightarrow 13$ rotational ladder of CH_3CN and in the $30_{4,26}$–$30_{3,27}$, and $32_{4,28}$–$32_{3,29}$ lines of SO_2. The peak of the velocity-integrated molecular emission is located $\sim 0\farcs4$ northwest of the peak of the continuum emission. The first-order moment images and channel maps show a velocity gradient of 1.1 km s^{-1} arcsec^{-1} across the source and a distinctive spot of blueshifted emission toward the peak of the zero-order moment. The rotational temperature is found to decrease from 252±24 K at the peak position to 166±16 K at its edge, indicating that our molecular observations are probing a hot molecular core that is internally excited. The emission in the H29α line arises from a region of $0\farcs65$ in size, where its peak coincides with that of the dust continuum. We model the kinematical characteristics of the "central blue spot" feature as due to infalling motions, suggesting a central mass of 172.8±8.8 $M_\odot$. Our observations indicate that this HC H II region is surrounded by a compact structure of hot molecular gas, which is rotating and infalling toward a central mass, that is most likely confining the ionized region. The observed scenario is reminiscent of a "butterfly pattern" with an approximately edge-on torus and ionized gas roughly parallel to its rotation axis.

Unified Astronomy Thesaurus concepts: Star formation (1569); Radio astronomy (1338); H II regions (694); Molecular clouds (1072); Molecular gas (1073)

1. Introduction

The formation of high-mass stars begins inside dense and massive molecular cores where high-mass protostellar objects accrete at rates between 10^{-5} and 10^{-3} $M_\odot$ yr^{-1} (Tan et al. 2014). These objects finish their Kelvin–Helmholtz (K–H) contraction very rapidly and reach the main sequence (Norberg & Maeder 2000; Keto & Wood 2006). At this point, the star radiates extreme-ultraviolet (UV) photons that ionize its surroundings, producing very small regions of ionized gas, observationally characterized by sizes $\leqslant$0.03 pc, densities $n_e > 10^6$ cm^{-3}, and emission measures (EMs) $> 10^8$ pc cm^{-6} (Kurtz 2000). These hypercompact (HC) regions are thought to signpost an early stage of the evolutionary path of high-mass young stellar objects (HMYSOs).

Theoretical calculations show that almost half of the mass of O-type stars is accreted after the K–H contraction and the onset of ionizing radiation (Hosokawa & Omukai 2009; Zhang et al. 2014). How high-mass stars keep accreting despite the onset of the ionizing radiation is not well established. Theoretical works have shown that, under steady spherical accretion, radiation pressure inhibits the growth of the protostars. An effective way to circumvent the radiation and ionized gas pressure is accretion from a disk, allowing the accreting material to reach the young high-mass stars much more easily by flowing inward, mainly through the plane perpendicular to the angular momentum vector of the system (Nakano 1989; Kuiper et al. 2011). Accretion through a disk may only choke the ionized region near the disk plane, allowing for H II region development in the polar regions (Keto 2007). In this scenario, an HC H II region should consist of an ionized biconical cavity confined by a rotating and contracting predominantly neutral molecular core.

How does accretion proceed after the onset of the ionizing radiation? How does the envelope material avoid being ionized

Table 1
Observational Parameters

Transition	Center Freq. (GHz)	Bandwidth (GHz)	Vel. Res. (km s^{-1})	Synthesized Beam (arcsec)	P.A. of the Synthesized Beams (deg)	rms Noise (mJy beam^{-1})
H29α	256.302035	1.875	1.320	0.52 × 0.40	–65.3	3.8
SO_2 v = 0 30(4,26)–30(3,27)	259.599448	0.23438	0.564	0.51 × 0.40	–64.9	4.4
SO_2 v = 0 32(4,28)–32(3,29)	258.388716	0.23438	0.566	0.51 × 0.40	–66.1	3.9
CH_3CN v = 0 14–13 ladder	257.325000	0.46875	0.569	0.52 × 0.40	–65.2	4.0

and blown away by its own pressure? To answer these questions, we undertook Atacama Large Millimeter/submillimeter Array (ALMA) Band 6 observations toward a set of luminous, embedded HMYSOs associated with HC HII regions in order to simultaneously observe molecular emission in highly excited transitions of SO_2 and CH_3CN and emission from the ionized gas in the H29α hydrogen recombination line (HRL). The two molecules have been used to trace velocity gradients, indicative of rotation, toward hot molecular cores around luminous, young, high-mass stars in several cases (e.g., Sánchez-Monge et al. 2013; Beltrán et al. 2014; Guzmán et al. 2014). Our molecular observations are intended to assess whether or not HC H II regions are associated with rotating hot molecular cores on scales of 3000 au, as well as to detect inflow motions from the surrounding gas. Our goal is to find evidence of disk accretion and to settle the question as to whether or not accretion onto the HMYSO is maintained after stellar contraction and UV photon injection.

In this work, we present observations toward the HC H II region G345.0061+01.794 B (hereafter G345.01 B; Guzmán et al. 2012) associated with IRAS 16533-4009. The Spitzer-GLIMPSE survey shows that it is associated with a bright, compact, mid-infrared source prominent in the 4.5 μm band. The G345.01 B HC H II region has the kinematic near and far distances of 1.7 and 14.7 kpc (Urquhart et al. 2007), respectively. The ambiguity can be resolved through spectrophotometric estimation (e.g., Guzmán et al. 2020). In this study, we adopt the spectrophotometric distance of 2.38 kpc (Moisés et al. 2011). Choosing the far distance not only results in an unrealistically massive cluster but also places it at an impractical distance above the Galactic plane.

The paper is organized as follows: in Section 2 we describe the observations performed with the ALMA; in Section 3 we present the observational results; in Section 4 we discuss the analysis of the data, including the physical relationship between the hot molecular core and the HC H II region; and in Section 5 we present a summary of the main points addressed in this paper.

2. Observations

We observed, using ALMA in Band 6 between 256.3 and 259.6 GHz, the dust continuum and molecular line emission toward the HC H II region G345.01 B (see Table 1). The observations were carried out, as part of ALMA Cycle 3, during 2016 May 21, using the 12 m array. The ALMA field of view at this wavelength is ∼22″, defined as the FWHM of the primary beam. The phase center of the array was (R.A., Decl., J2000) = ($16^h56^m47^s$, −40°14′25″). We observed four spectral windows in dual polarization mode. The first window was centered at the frequency of 256.302035 GHz and has a bandwidth of 1875.00 MHz and a spectral resolution of 1.129 MHz. This setup was chosen to map the H29α radio recombination line (RRL) emission from the HC II region. The second and third windows were centered, respectively, at the frequencies of 258.388716 and 259.599448 GHz each with 234.38 MHz bandwidths and 488.281 kHz (∼0.564 km s^{-1}) channels. These two setups were chosen to observe the emission from the purported hot core in two high-excitation temperature lines of SO_2. The fourth window, centered at the frequency of 257.325000 GHz, has a bandwidth of 468.75 MHz and a resolution of 488.281 kHz. This setup was chosen to observe the emission of CH_3CN, a good temperature probe of both the large-scale diffuse and small-scale dense gas, in the $J = 14$–13 ladder. Zapata et al. (2015) point out that, based on the analysis of IRAS 16547-4247, to detect emission from the inner regions of the rotating core, it is important to use molecular transitions with high upper energy levels (> 300 K). The selected SO_2 transitions, $30_{4,26}$–$30_{3,27}$ and $32_{4,28}$–$32_{3,29}$, have upper level temperatures of 471 and 531 K, respectively, and those of the lines in the CH_3CN 14–13 ladder range between 92 and 670 K.

J1427-4206 was used as a bandpass calibrator, J1717-3342 was observed as a phase calibrator, and J1617-5848 was measured as a flux calibrator. Table 1 lists the parameters of each spectral window, the synthesized beams, and the rms noise achieved. The integration time on source was 35 minutes. Calibration and reduction of these data were done using the Common Astronomy and Software Applications (CASA; McMullin et al. 2007).

The continuum was subtracted by selecting the line-free channels from the visibilities using the CASA task uvcontsub. These line-free channels in turn were used to create the continuum images directly in tclean.

3. Results

3.1. Molecular Emission

3.1.1. CH_3CN

Figure 1 presents the spectrum of the emission in the $J = 14 \rightarrow 13$ rotational transition of CH_3CN integrated over a region of 0.″5 in diameter, centered on the G345.01 B HC H II region. Other lines are also present. The stronger ones are indicated in Figure 1 and briefly addressed in Section 4.3. Their transitions, line frequencies, and upper-state energy levels are given in Table 2. The $J = 14 \rightarrow 13$ rotational transition of CH_3CN consists of 14 K components ($K = 0$, 1, ...13; K being the projection of the total angular momentum of the molecule onto its principal rotation axis), of which ten lie within the observed spectral window (red dotted lines).

Figure 2 displays images of the zero-order (upper panels) and first-order moments (lower panels) of the emission in the $K = 2$, 3, 4, 6, 7, and 8 components of the $J = 14$–13 ladder of CH_3CN. Moments of the $K = 0$, 1, 5, and 9 components are not shown since they are blended with each other or with other

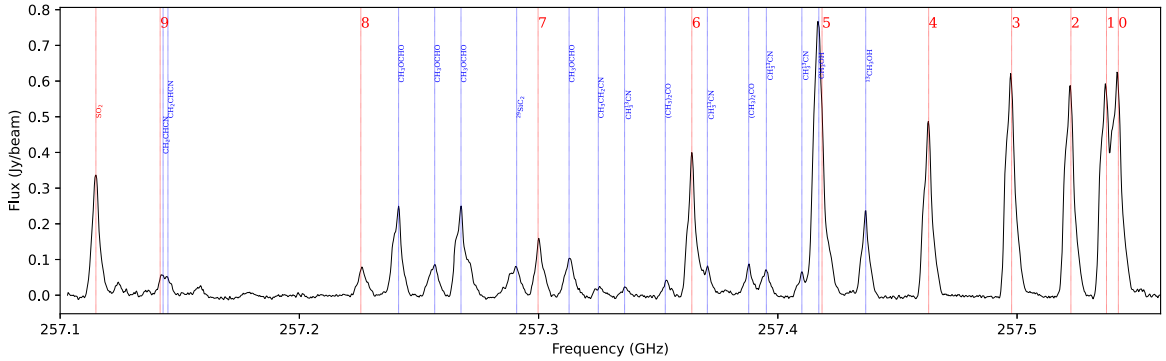

Figure 1. Spectra of the methyl cyanide emission, integrated over a region of 0.″5, centered on the G345.01 B HC H II region. K components of the CH_3CN 14–13 transition are marked with red dotted lines ($V_{LSR} = -14$ km s^{-1}). In addition, some other lines detected in this spectral window are marked with blue dashed lines.

Table 2
Observational Parameters of CH_3CN $J = 14 \rightarrow 13$ Rotational Lines and Other Lines Detected in This Spectral Window

Species	Transition	Frequency (GHz)	E_u/k (K)
CH_3CN	$14_0 \rightarrow 13_0$	257.527	92.70
	$14_1 \rightarrow 13_1$	257.522	99.85
	$14_2 \rightarrow 13_2$	257.508	121.28
	$14_3 \rightarrow 13_3$	257.483	156.99
	$14_4 \rightarrow 13_4$	257.448	206.98
	$14_5 \rightarrow 13_5$	257.404	271.23
	$14_6 \rightarrow 13_6$	257.349	349.72
	$14_7 \rightarrow 13_7$	257.285	442.45
	$14_8 \rightarrow 13_8$	257.210	549.38
	$14_9 \rightarrow 13_9$	257.127	670.50
$^{13}CH_3OH$	15(3,13)–15(2,14) +−	257.422	321.79
CH_3OH	18(3,16)–18(2,17) +−	257.402	446.53
$CH_3^{13}CN$	14(1)–13(1), F = 14–13	257.393	99.80
	14(2)–13(2), F = 14–13	257.380	121.23
	14(3)–13(3), F = 14–13	257.355	156.94
	14(4)–13(4), F = 14–13	257.321	206.93
$(CH_3)_2CO$	24(3,22)–23(3,21) EE	257.373	165.68
	24(3,22)–23(2,21) AE	257.338	165.75
CH_3CH_2CN	30(0.30)–29(0,29)	257.310	193.54
CH_3OCHO	21(9,13)–20(9,12)A	257.298	377.19
	23(2,22)–22(2,21)E	257.242	342.23
	20(5,15)–19(5,14)E	257.227	142.79
CH_3OCHO	20(5,15)–19(5,14)A	257.253	142.79
$^{29}SiC_2$	11(4,8)–10(4,7)	257.276	105.23
SO_2	7(3,5)–7(2,6)	257.100	47.84

molecular lines (see Figure 1). Superimposed are contours of the continuum emission. The peak of the velocity-integrated intensity CH_3CN emission is located $\sim 0.''4 \pm 0.''1$ northwest of the peak of the continuum emission. The first-order moment images show a velocity gradient from roughly east to west with average velocities preferentially blueshifted on the western side and redshifted on the eastern side. A spot of blueshifted emission is seen toward the peak of the zero-order moment. The "blue spot" feature is present in all K components shown in Figure 2, confirming that its detection is a robust result.

Figure 3 presents channel maps of the emission in the $K = 3$ component, which clearly exhibits the shift in velocity, from blueshifted velocities in the west to redshifted velocities in the east. Additionally, a "butterfly pattern" is also noteworthy, which may indicate the presence of accretion disks around high-mass stars.

The "blue spot" feature and a velocity change are illustrated in Figure 4, which presents position–velocity diagrams of the emission in the $K = 0$, 1, 2, and 3 components along a direction from the red part to the blue part, with a position angle (P.A.) of 255° passing through the continuum peak. There is a clear change in velocity across the source of 4.3 km s^{-1} over a region of 3.″8 (equivalent to 98 km s^{-1} pc^{-1} at a distance of 2.38 kpc). If this velocity gradient is due to gravitationally bound rotation, it implies a dynamical mass within a 0.023 pc radius of 51 $M_\odot$, less than half the mass of the central object as derived in Section 4.3. We conclude that the hot molecular gas is likely bound and rotating around the central object.

3.1.2. SO_2

In addition to the high-excitation lines of SO_2 observed on purpose in this work, the spectral window of the RRL encompasses four additional transitions of SO_2, all of which connect levels with less than 50 K above the ground state. The transitions and their parameters are listed in Table 3; column (2) gives the frequency, column (3) gives the energy of the upper state, column (4) gives the Einstein A coefficient, and column (5) gives the statistical weight of the upper state.

Figure 5 shows images of the velocity-integrated intensity (upper panels) and intensity-weighted velocity (moment 1; lower panels) in all six observed SO_2 lines, in order of increasing excitation temperature. The peak position of the integrated intensity in SO_2 is similar (<0.″01) to that in the CH_3CN lines. The "blue spot" signature is also present in the SO_2 moment-one maps.

3.2. Ionized Gas: H29α RRL Emission

Since at Band 6 frequencies the continuum is likely to be dominated by dust emission, HRLs become the most direct way to trace the ionized gas. Figure 6 (left panel) shows an image of the velocity-integrated H29α emission along with the dust continuum contours. Intensities were integrated from $V_{LSR} = -44$ to 8 km s^{-1}. The position of the peak in the velocity-integrated line emission, of 18.7 Jy beam^{-1} km s^{-1}, is coincident with that of the dust continuum (R.A., decl.) (J2000) $=(16^h56^m47.6\pm0.^s1, -40°14'26.''07\pm0.10)$.

A Gaussian fit to the observed H29α brightness distribution indicates that the HC HII region has a deconvolved angular size (FWHM) $\theta_s = \sqrt{0.''75 \times 0.''56} \approx 0.''65$, corresponding to the geometrical mean of the deconvolved major and minor axes. At the distance of 2.38 kpc, this implies a diameter of 0.0075 pc.

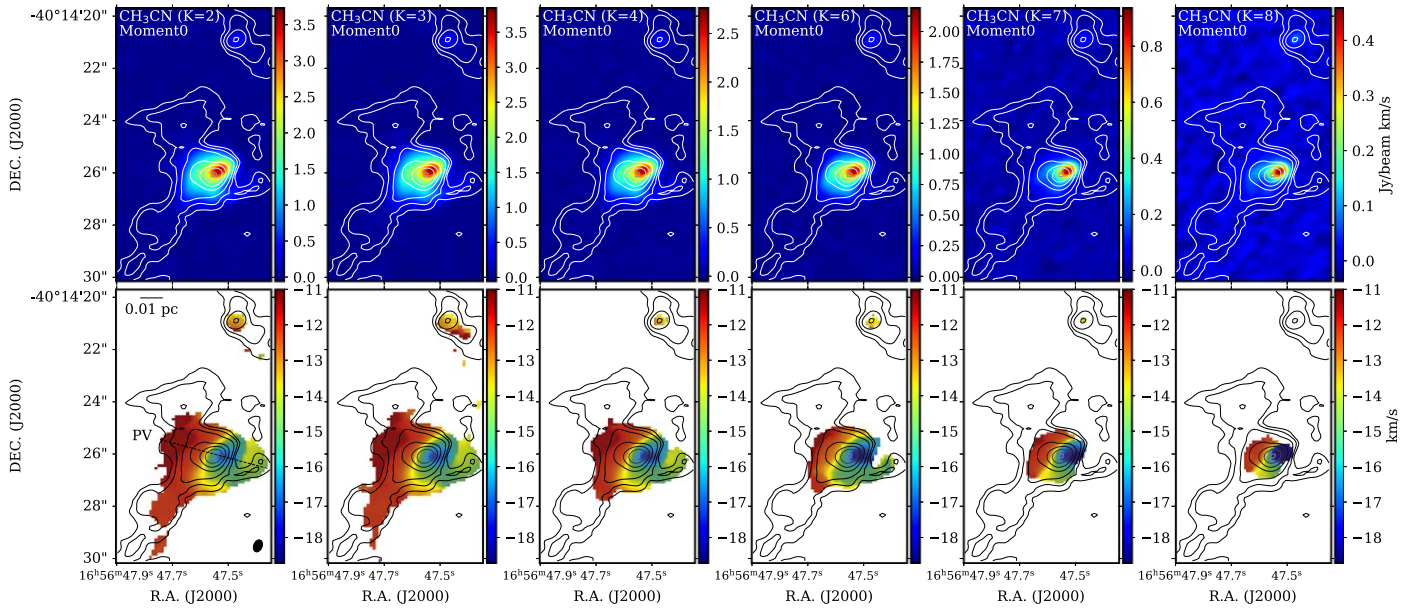

Figure 2. Images of the velocity-integrated intensity (moment 0; upper panels) and intensity-weighted velocities (moment 1; lower panels) in the CH_3CN $J = 14$–13 $K = 2$, 3, 4, 6, 7, and 8 transitions toward the G345.01 B HC H II region. Superimposed are contours of the continuum emission. Contour levels are 10σ, 20σ, 40σ, 100σ, 200σ, 400σ, and 800σ, where σ is 0.3 mJy beam^{-1}. The black dashed line shown in the lower left panel indicates the position of the position–velocity cut mentioned in Section 3.1.1. The black ellipse shown at the bottom right corner of the lower left panel indicates the beam size.

Figure 6, right panel, shows a spectrum of the H29α RRL emission integrated over the source. A Gaussian fit to the line profile gives a line width of 33.7 ± 2.3 km s^{-1} and a line-center velocity of $V_{\rm LSR} = -18.1 \pm 0.9$ km s^{-1}. This velocity differs from those of the CH_3CN and SO_2 molecular lines. It may be due to the fact that ionized gas and molecular cloud are slightly displaced.

The electron temperature T_e^* can be derived from the following expression (Gordon & Sorochenko 2002) assuming local thermodynamic equilibrium (LTE) conditions:

$$T_e^* = \left[\left(\frac{6985}{\alpha(\nu, T_e)}\right)\left(\frac{\Delta V_{\rm H29\alpha}}{\rm km\ s^{-1}}\right)^{-1}\left(\frac{S_{\rm ff}}{S_{\rm H29\alpha}}\right)\left(\frac{\nu}{\rm GHz}\right)^{1.1} \times\left(1 + \frac{N({\rm He^+})}{N({\rm H^+})}\right)^{-1}\right]^{0.87}, \quad (1)$$

where $S_{\rm ff}$ is the free–free continuum flux density, $S_{\rm H29\alpha}$ is the H29α peak flux density, $\alpha(\nu, T_e) \sim 1$ is a slowly varying function of frequency (Mezger & Henderson 1967), and $N({\rm He^+})/N({\rm H^+})$ is the He^+ to H^+ abundance ratio. The free–free flux density, $S_{\rm ff}$, cannot be derived from the continuum emission at 256 GHz because of the contribution of dust emission at this frequency. We estimate it using the parameters of the HC HII region (EM and size) derived by Guzmán et al. (2012), from a fit to the observed radio continuum spectra at lower frequencies, obtaining a value of $S_{\rm ff} = 325 \pm 65$ mJy. Using the observed values of $S_{\rm H29\alpha} = 883 \pm 47$ mJy and $\Delta V_{\rm H29\alpha} = 33.7 \pm 2.3$ km s^{-1} and adopting a value of 0.096 for the He^+ to H^+ abundance ratio (Mehringer 1994), we get an electron temperature $T_e^* = 8094 \pm 1534$ K.

Further parameters of the region of ionized gas can be computed using the equations presented in Mezger & Henderson (1967) and Mezger et al. (1974). Assuming that the HII region is spherical and homogeneous, using the values of the continuum flux density at 256 GHz (325 ± 65 mJy), the angular size ($0\farcs65$), electron temperature (8094 ± 1534 K), and distance (2.38 kpc), we determine an electron density of $(2.1 \pm 0.2) \times 10^5$ cm^{-3}, an EM of $(4.6 \pm 0.9) \times 10^8$ pc cm^{-6}, a mass of ionized gas $(3.6 \pm 0.3) \times 10^{-3}$ $M_\odot$, and the number of ionizing photons required to excite the H II region becomes $(2.6 \pm 0.6) \times 10^{47}$s^{-1}. The errors neither include the distance uncertainty nor potentially strong density gradients as suggested by Kurtz et al. (2000). If we consider the near and far distances of 1.7 and 14.7 kpc, the inferred Lyman continuum flux suggests the presence of a massive star equivalent to a zero-age main-sequence star of type B0 and O5.5, respectively, within the G345.01 B HC H II region (Panagia 1973) which corresponds to a stellar object with a mass of 10 $M_\odot$ to 30 $M_\odot$.

Table 3
Parameters of the Observed SO_2 Transitions

Transitions	Frequency (GHz)	E_u/k (K)	$A_{\rm ul}$ (10^{-4} cm^{-1})	$g_{\rm u}$
High-excitation Lines				
$30_{4,26}$–$30_{3,27}$	259.599	471.50	2.07	61
$32_{4,28}$–$32_{3,29}$	258.389	531.10	2.1	65
Low-excitation Lines				
$3_{3,1}$–$3_{2,2}$	255.958	27.62	0.66	7
$4_{3,1}$–$4_{2,2}$	255.553	31.29	0.93	9
$5_{3,3}$–$5_{2,4}$	256.247	35.89	1.07	11
$7_{3,5}$–$7_{2,6}$	257.100	47.84	1.22	15

3.3. Dust Continuum

Continuum contours are overlaid on all moment maps depicting CH_3CN, SO_2, and H29α RRL in Figures 2, 3, 5, and 6(a). Continuum contour levels are set at 10σ, 20σ, 40σ, 100σ, 200σ, 400σ, and 800σ, with σ being 0.3 mJy beam^{-1}. The peak position, measuring 0.234 Jy beam^{-1}, aligns ($<0\farcs01$) with that of the ionized gas (H29α RRL), while the peak of the velocity-

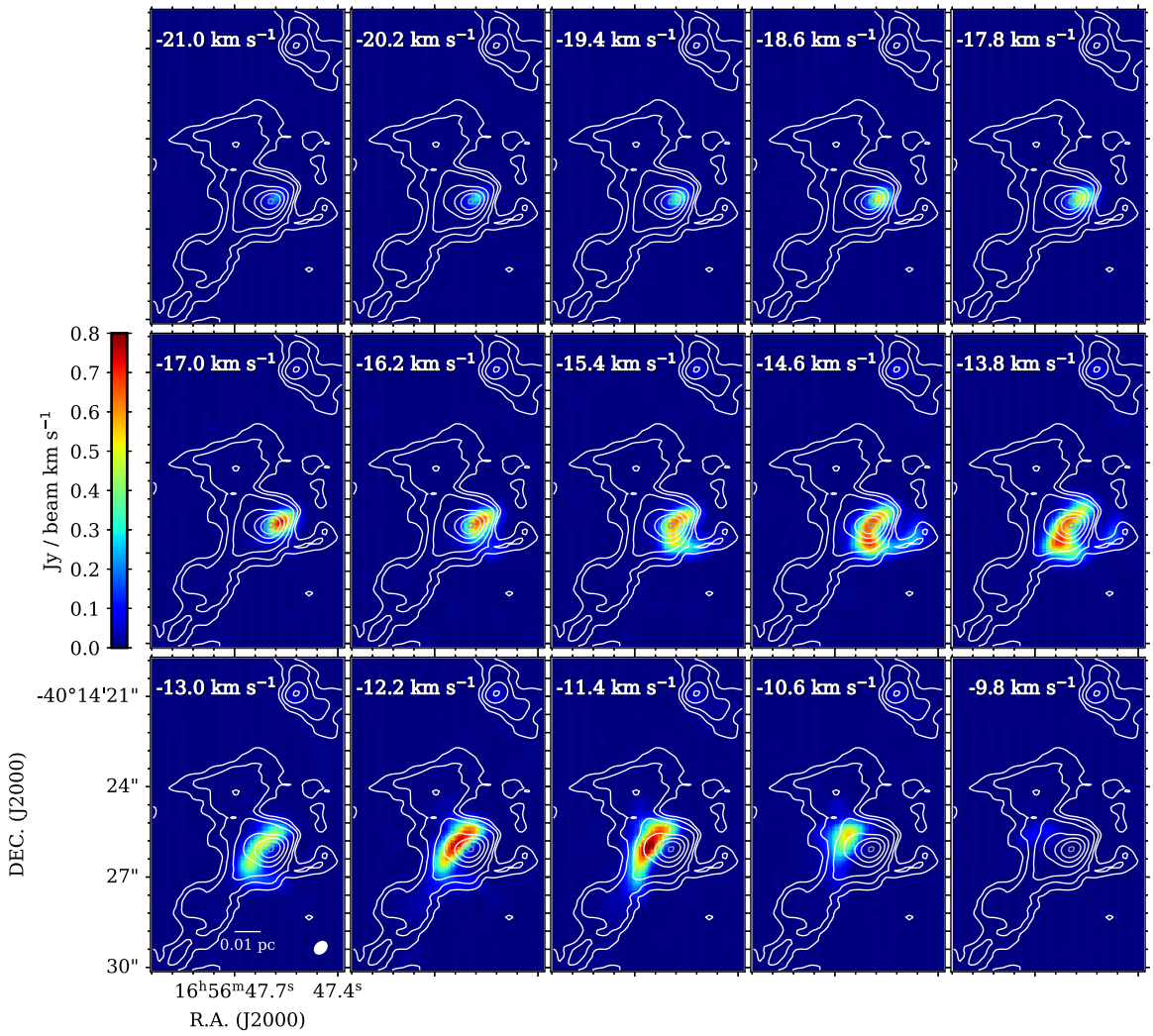

Figure 3. Channel maps for the $K = 3$ component of the CH_3CN $J = 14$–13 transition. The contours provide the continuum emission already presented in Figure 2. The white ellipse shown in the lower right corner of the bottom left panel indicates the beam size.

integrated intensity of CH_3CN and SO_2 emissions is situated (as mentioned before) approximately 0.″4 northwest of the continuum emission peak. We estimate the dust continuum flux of 565 ± 112 mJy by subtracting the contribution of the free–free emission of 325 ± 65 mJy from the total flux of the continuum map of 890 ± 47 mJy.

The mass of the core (central star) is obtained from the following equation using the dust continuum flux:

$$M_{\rm dust} = \frac{S_{1.1\rm mm} \times D^2}{k_{1.1\rm mm} \times B_{1.1\rm mm}(T_{\rm dust})}, \quad (2)$$

where $S_{1.1\rm mm}$ is the dust continuum flux, D is the distance to the object, and $T_{1.1\rm mm}$ is the dust temperature. $B_{1.1\rm mm}(T_{\rm dust})$ represents the Planck function (blackbody radiation) at the dust temperature $T_{\rm dust}$, and we adopt a grain emissivity, $k_{1.1\rm mm} = 0.0078$ cm^2 g^{-1}, which is the value calculated by Ossenkopf & Henning (1994) for bare grains and dense gas, where a gas-to-dust ratio of 100 is assumed. Adopting $T_{\rm dust} = 250$ K (see Section 4.1), we derive a dust mass of $\sim 4\ M_\odot$ (for a distance of 2.38 kpc). This dust mass is significantly smaller than the mass of the central object as derived in Section 4.3, while its gas mass is larger. We conclude that the gravitational field is significantly influenced by the central star.

4. Discussion

4.1. Rotational Temperature of CH_3CN

Rotational temperature and total column density of CH_3CN were derived from the Madrid Data Cube Analysis (MADCUBA;[15] Martín et al. 2019) software assuming LTE.

Figure 7 displays rotational diagrams of the emission at the peak position ("blue spot" in Figure 2) and in half rings going from the peak position toward the southeast (diameters at P.A.s of 135°) with different radii (R_1–R_5) from the peak position. The rings are centered at the peak position and have widths of 0.″15. The inner ring (R1) has an inner radius of 0.″33. The rotational temperature decreases outwards with distance from the "blue spot" (exciting star), being 252±24 K at the peak position and 166±16 K at the edge of the molecular (CH_3CN) structure (∼0.01 pc). Figure 8 plots the computed rotational temperature versus the projected distance from the "blue spot."

[15] MADCUBA is a software developed in the Madrid Center of Astrobiology (INTA-CSIC), which enables to visualize and analyze single spectra and data cubes: https://cab.inta-csic.es/madcuba/.

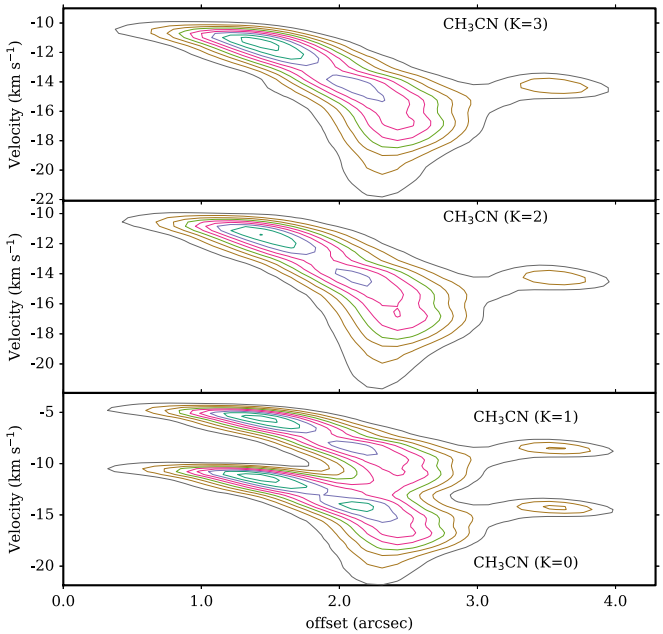

Figure 4. Position–velocity diagrams of $K = 0$, 1, 2, and 3 components of the CH_3CN $J = 14$–13 transition along a direction from the red to the blue part, with a position angle (P.A.) of 255° passing through the continuum peak (see Figure 2). Contour levels are 10%, 20%, 30%, 40%, 50%, 60%, 70%, 80%, and 90% of the peak value of 0.7 Jy beam^{-1}.

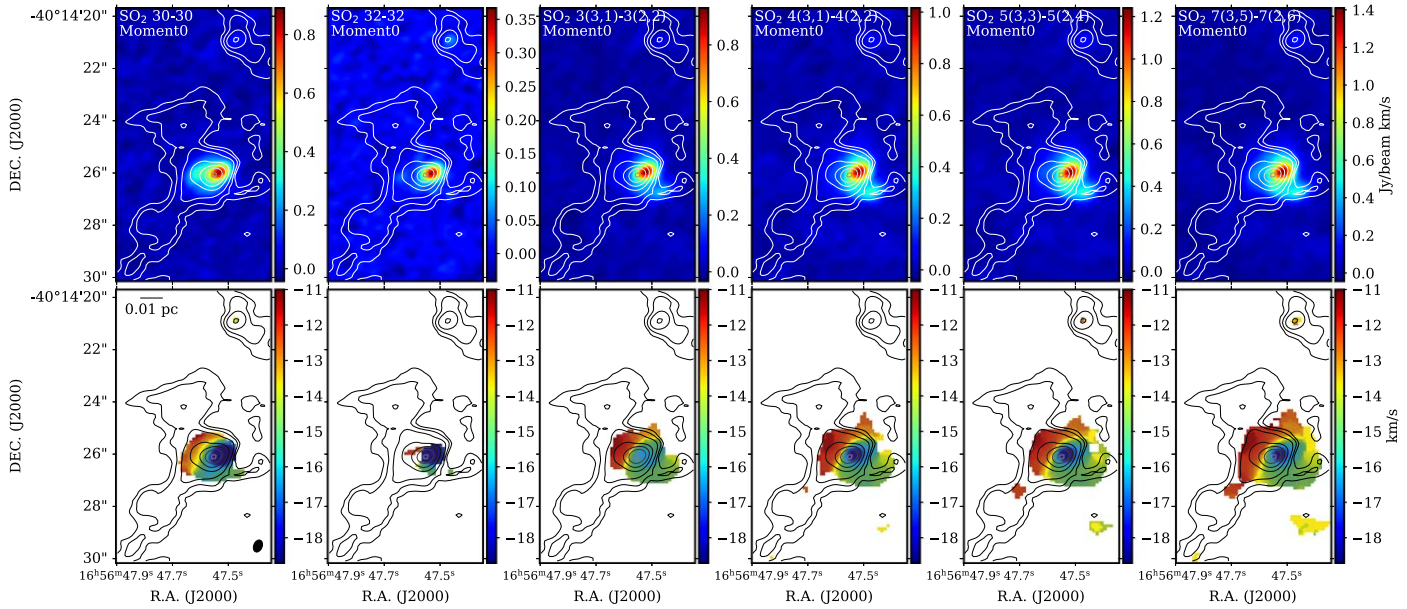

Figure 5. Same as Figure 2 for $30_{4,26}$–$30_{3,27}$; $32_{4,28}$–$32_{3,29}$; $3_{3,1}$–$3_{2,2}$; $4_{3,1}$–$4_{2,2}$; $5_{3,3}$–$5_{2,4}$; and $7_{3,5}$–$7_{2,6}$ SO_2 emissions.

A power-law fit to the observed dependence gives $T_{\rm rot} = 154\, r^{-0.35\pm0.19}$. This result suggests that the molecular gas is heated via collisional excitation with hot dust, which in turn is heated by the absorption of radiation emitted by the central star (Scoville & Kwan 1976). Using Expression (11) in Garay & Lizano (1999), we infer that the power-law index of dust emissivity at far-infrared wavelengths, β, is 0.55 with an emissivity, f, of 0.08 and that the luminosity of the central object is $1.1 \times 10^4\ L_\odot$. This luminosity is in good agreement with the luminosity of the star ionizing the HC H II region as determined by Guzmán et al. (2012) from radio continuum observations.

4.2. Rotational Temperature of SO_2

From the emission of the four low-excitation lines of SO_2 shown in Table 3, we obtain the rotational temperature of the envelope with MADCUBA. Figure 9 plots a rotational diagram of emission from the whole region. A linear fit to the observed trend implies a temperature of 40 ± 6 K. Since the data are well matched by a linear fit, all SO_2 lines appear to be optically thin.

4.3. Infall Motions

Within the spectral window covered by the ALMA data (see Figure 1), additional spectral features are also detected. Not

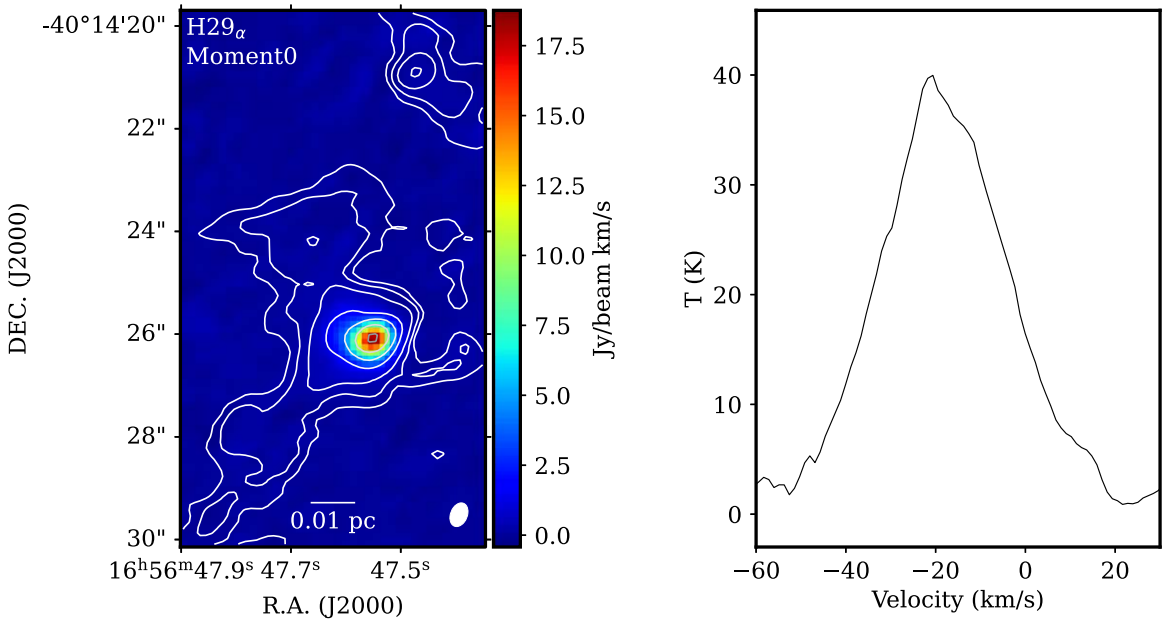

Figure 6. Left panel: an image of the velocity-integrated H29α RRL emission along with the dust continuum contours (see Figure 2). Right panel: a spectrum of the H29α RRL emission integrated over the source. A Gaussian fit to the line profile gives a line width of 33.7 ± 2.3 km s^{-1} and a line-center velocity of $V_{\rm LSR} = -18.1 \pm 0.9$ km s^{-1}.

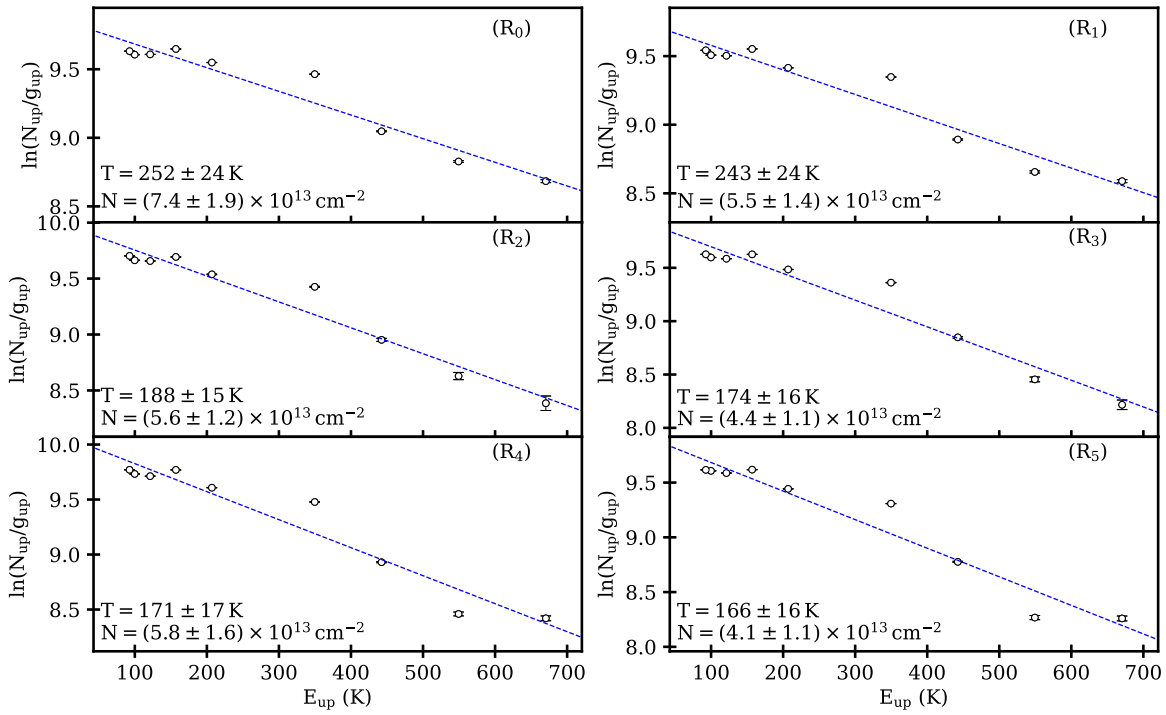

Figure 7. Rotational diagrams of CH_3CN derived from the peak position ("blue spot," in lower panels of Figure 2) and in half rings going from the peak position toward the southeast (P.A.: 135°) with different radii (R_1 to R_5) from the peak position using MADCUBA. The rings are centered at the peak position and have widths of 0.″15. The inner ring ($R1$) has an inner radius of 0.″33. The rotational temperature decreases from the peak position to the edge of the source ($\sim$1″) from 252±24 to 166±16 K.

only the line profiles of CH_3CN and SO_2 but also the lines of other species such as CH_3OCHO and $^{13}CH_3OH$, integrated over a region of 0.″5 in size and centered on the G345.01 B HC HII region, show a blue asymmetry in their line profiles. Figure 10 shows the observed line profiles of several K components of the CH_3CN $J = 14$–13 transition (marked with red dashed lines) toward the "blue spot" position. These spectra also show a blue asymmetry in their line profiles. The appearance of the line profiles is consistent with the detection of the "classic" asymmetric-line profile-infall signature (Narayanan et al. 1998). Furthermore, Mayen-Gijon et al. (2014) and Estalella et al. (2019) suggested that the "blue spot" feature mentioned above (see Section 3.1) is a clear signature of infall. The observation of a blue spot, coupled with the absence of a corresponding red spot, aligns well with the proposed infall scenario. This discrepancy can be attributed to the obscuration

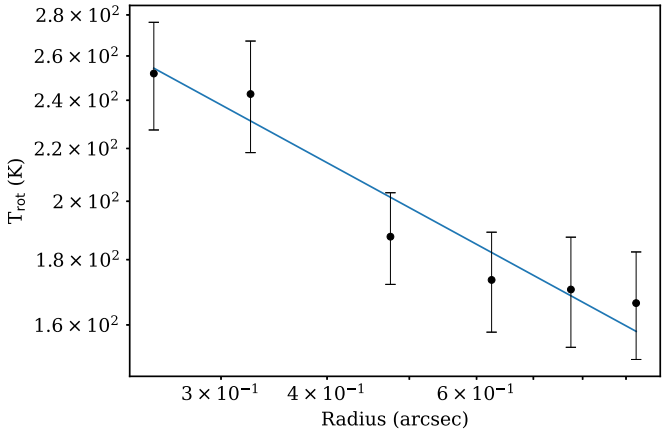

Figure 8. Rotational temperature of the CH_3CN versus projected distance from the "blue spot" (see the lower panels in Figure 2). A power-law fit to the observed dependence gives $T_{\rm rot} = 154\ r^{-0.35\pm0.19}$.

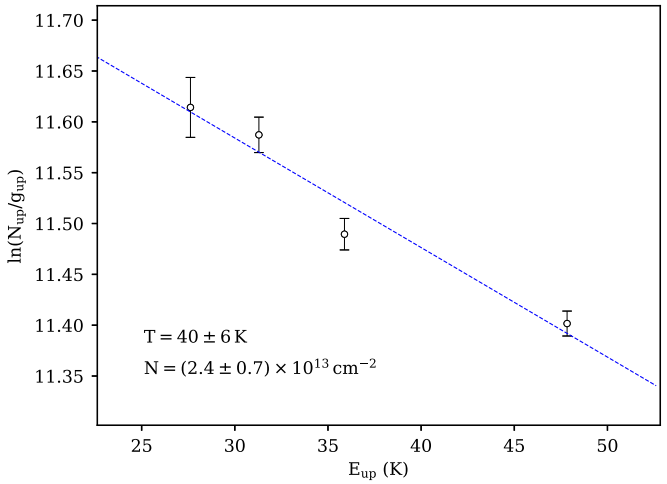

Figure 9. Rotational diagram using the emission from the low-excitation lines of SO_2 integrated over the whole source. A linear fit to the observed trend implies an excitation temperature of 40 ± 6 K.

of the putative red spot, which lies adjacent to and directly in front of the stellar object, by more extended redshifted gas situated in the foreground. The central region of the first-order map appears blueshifted because the blueshifted emission, arising from gas close to and mainly behind the central stellar object, is stronger than the redshifted emission from gas farther away and in front of the stellar object. This asymmetry is produced when the optical depth is high enough so that at a given line-of-sight velocity, the gas facing the observer hides the emission from the gas behind it (Anglada et al. 1987, 1991).

At larger distances from the center, the integrated intensity decreases, the blue- and redshifted intensities become similar, and the intensity-weighted mean velocity approaches the systemic velocity of the cloud. Therefore, the first-order moment of an infalling envelope is characterized by a compact spot of blueshifted emission toward the position of the zeroth-order moment peak.

In order to determine the infall velocity, central mass, and infall radius, we use the hallmark model of Estalella et al. (2019). The value of the first-order moment as a function of the angular distance was obtained for the unblended K components of the $J = 14$–13 transition of CH_3CN by averaging the first-order moment in concentric rings of width $0\farcs05$ centered on the average position of the peak of the "blue spot," (R.A., decl.) (J2000) = ($16^{\rm h}56^{\rm m}47\fs6$, $-40°14'25\farcs98$). The first-order moment profiles of the different components are presented in Figure 11. They seem to belong to two separate groups, with the first-order moment values for the $K = 2$, 3, and 4 components being higher than those of the $K = 6$, 7, and 8 components, especially near the peak position. However, the $K = 7$ component follows the $K = 2$, 3, and 4 components beyond $0\farcs5$ distance from the peak. The difference is likely due to the higher-K lines probing the hotter gas close to the HC H II region. The best fit is obtained for an infall radius much larger than the beam size, an ambient-gas velocity of $V_{\rm LSR} = -12.49 \pm 0.16$ km s^{-1}, and a central mass of $172.8 \pm 8.8\ M_\odot$ (for a distance of 2.38 kpc, and the error does not include the distance uncertainty). To ensure accuracy and assess sensitivity of the model to distance variations, we also fit this model using the near distance of 1.7 kpc, and we get an ambient-gas velocity of $V_{\rm LSR} = -12.46 \pm 0.16$ km s^{-1} and a central mass of $126.0 \pm 8.7\ M_\odot$. This central mass is much larger than that derived from the number of Lyman photons presented in Section 3.2. This difference could be attributed to forming a very massive star, which is still undergoing infall, emitting fewer ionizing photons than a main-sequence star of the same mass. The clear detection of the "central blue spot" signature in the G345.0061+01.794 B HC H II region indicates that infall motions play a fundamental role in the gas kinematics of this source.

4.4. Butterfly Pattern

In the channel maps (in Figure 3) a "butterfly pattern"–like structure is observed. The body of the butterfly, a potentially inflated rotating torus, showing redshifted emission in the east and blueshifted one in the west, extends across the center of the source. Roughly parallel to the rotation axis of this torus we find ionized gas on both sides, i.e., in the north and south. The extent and thickness of the torus are similar, and the ionized gas in the north is oriented slightly eastwards, and the one in the south is also oriented somewhat eastwards. Hence, the butterfly pattern is not perfectly fulfilled, but the observational data come close to it. Apparently, we see the source from a suitable viewing angle, i.e., the torus is seen approximately edge-on.

5. Conclusion

We carried out high angular resolution observations, using ALMA, of emission in highly excited molecular lines of CH_3CN and SO_2 and in the H29α RRL toward the G345.0061+01.794 B HC H II region. The main results and conclusions are summarized as follows:

1. Emission was detected in all ten observed K components of the $J = 14 \rightarrow 13$ rotational ladder of CH_3CN and in the $30_{4,26}$–$30_{3,27}$ and $32_{4,28}$–$32_{3,29}$ lines of SO_2. The peak of the velocity-integrated molecular line intensity is located slightly NW (about $0\farcs4 \pm 0\farcs1$) of the peak of the continuum emission.
2. The first-order moment images of the molecular emission show a central spot of blueshifted emission, with respect to the systemic velocity of the cloud, located at the peak of the zero-order moment, seen in all K components of CH_3CN, in the SO_2 lines and in transitions of other species serendipitously detected in the measured frequency band.

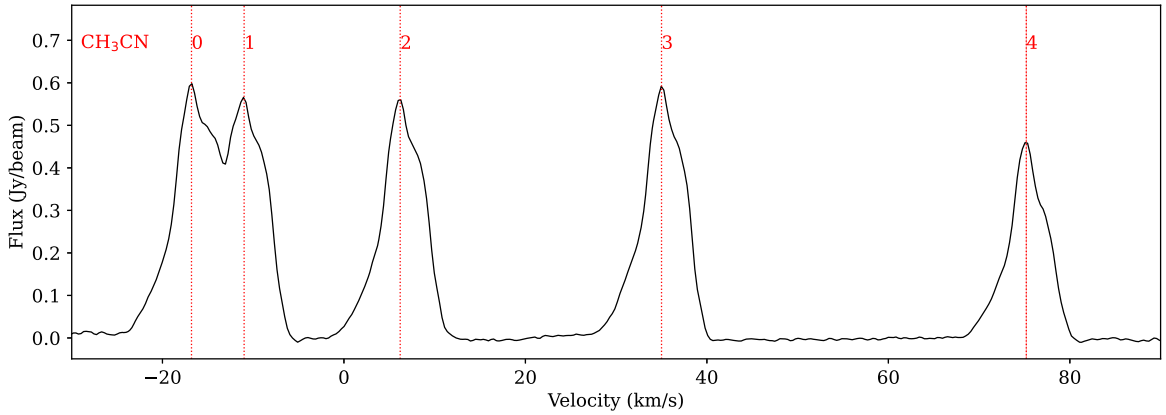

Figure 10. Observed line profiles of several K components of the CH_3CN $J = 14$–13 transition (marked with red dashed lines) toward the "blue spot" position (the angular size is $\sim 0\farcs4$, $V_{LSR} = -17$ km s^{-1}).

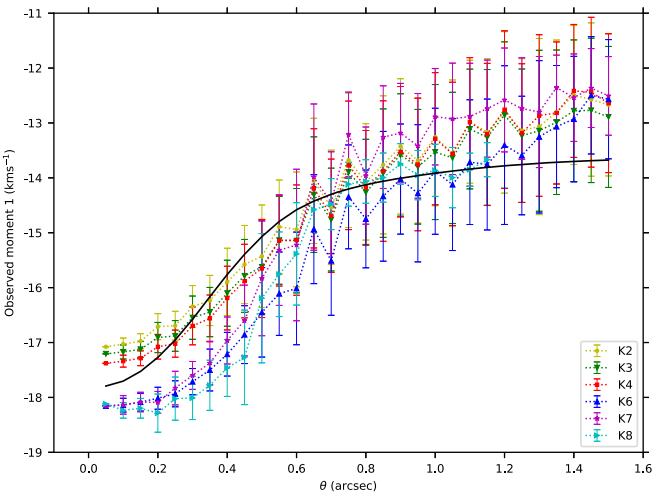

Figure 11. G345.01 first-order moment for the CH_3CN transitions as a function of angular distance, measured for full rings of width $0\farcs05$ centered on the average position of the peak of the "blue spot," (R.A., decl.) (J2000) = ($16^h56^m47\fs6$, $-40°14'25\farcs98$), and average radius θ. The error bars are the standard deviation of uncertainties of the velocity inside each ring. The black solid line shows the best fit to the data. The best fit is obtained for an infall radius much larger than the beam size, an ambient-gas velocity $V_{LSR} = -12.49 \pm 0.16$ km s^{-1}, and a central mass of 172.8 ± 8.8 $M_\odot$ (for a distance of 2.38 kpc).

3. Rotational diagrams of the emission of the methyl cyanide lines show that the rotational temperature has a peak value of 252±24 K at the position of the "blue spot" and decreases outwards, reaching a value of 166±16 K at the edge ($\sim 1''$, 0.01 pc for a distance of 2.38 kpc) of the molecular structure, indicating that our observations are probing a hot molecular core that is internally excited. In addition, from the emission of four low-excitation lines of SO_2, we estimate a rotational temperature of 40 ± 6 K for the envelope integrated over the whole source.
4. The first-order moment images and channel maps of the molecular emission show a velocity gradient from roughly east to west with average velocities preferentially blueshifted on the western and redshifted on the eastern side. The change in velocity amounts to 4.3 km s^{-1} over a region of $3\farcs8$ (equivalent to 98 km s^{-1} pc^{-1} at the distance of 2.38 kpc).
5. Emission was detected in the H29α line, having a line-center velocity of $V_{LSR} = -18.1 \pm 0.9$ km s^{-1} and a line width (FWHM) of 33.7 ± 2.3 km s^{-1}. The position of the peak in the velocity-integrated emission is coincident with that of the dust continuum. The RRL observations indicate that the ionized gas emission arises from a region having a radius of 0.0037 pc, a mass of ionized gas of $(3.6 \pm 0.3) \times 10^{-3}$ $M_\odot$, an electron temperature of 8094 ± 1534 K, an EM of $(4.6 \pm 0.9) \times 10^8$ pc cm^{-6}, and an electron density $(2.1 \pm 0.2) \times 10^5$ cm^{-3} (for a distance of 2.38 kpc).
6. We modeled the kinematical characteristics of a "central blue spot" feature as due to infalling motions, deriving a central mass of 172.8 ± 8.8 $M_\odot$ (for a distance of 2.38 kpc). We conclude that the HC H II region is surrounded by a compact structure of hot molecular gas, which is rotating and infalling toward a central mass of 172.8 ± 8.8 $M_\odot$, which is most likely confining the region of ionized gas.
7. The properties for the source are reminiscent of the theoretically proposed "butterfly pattern," with the rotating torus seen almost edge-on and the ionized gas extending roughly perpendicular to it.

Acknowledgments

The authors would like to express their sincere gratitude to Eric Keto for critical evaluation of the paper. This research was funded by the Science Committee of the Ministry of Science and Higher Education of the Republic of Kazakhstan (grant Nos. AP13067768 and AP14870504) and sponsored (in part) by the Chinese Academy of Sciences (CAS), through a grant to the CAS South America Center for Astronomy (CASSACA) in Santiago, Chile. G.G. acknowledges support from ANID BASAL project FB210003. R.E. acknowledges partial financial support from the grants PID2020-117710GB-I00 and CEX2019-000918-M funded by MCIN/ AEI /10.13039/501100011033. J.E. acknowledges support from the National Key R&D Program of China under grant No.2022YFA1603103 and the Regional Collaborative Innovation Project of Xinjiang Uyghur Autonomous Region grant 2022E01050. D.L. acknowledges support from National Natural Science Foundation of China (NSFC) through grant No. 12173075 and support from Youth Innovation Promotion Association CAS. Y.H. acknowledges support from the CAS "Light of West China" Program under grant No. 2020-XBQNXZ-017 and the Xinjiang Key Laboratory of Radio Astrophysics under grant No. 2023D04033. This paper

makes use of the following ALMA data: ADS/JAO. ALMA#2015.1.01371.S. ALMA is a partnership of ESO (representing its member states), NSF (USA) and NINS (Japan), together with NRC (Canada), MOST and ASIAA (Taiwan), and KASI (Republic of Korea), in cooperation with the Republic of Chile. The Joint ALMA Observatory is operated by ESO, AUI/NRAO and NAOJ.

Facility: ALMA.

Software: astropy (Astropy Collaboration et al. 2013, 2018), CASA (McMullin et al. 2007), MADCUBA (Martín et al. 2019).

ORCID iDs

Toktarkhan Komesh https://orcid.org/0000-0002-3415-4636
Christian Henkel https://orcid.org/0000-0002-7495-4005
Robert Estalella https://orcid.org/0000-0001-7341-8641
Yuxin He https://orcid.org/0000-0002-8760-8988

References

Anglada, G., Estalella, R., Rodriguez, L. F., & Lopez, J. C. R. 1991, A&A, 252, 639
Anglada, G., Rodriguez, L. F., Canto, J., Estalella, R., & Lopez, R. 1987, A&A, 186, 280
Astropy Collaboration, Price-Whelan, A. M., Sipőcz, B. M., et al. 2018, AJ, 156, 123
Astropy Collaboration, Robitaille, T. P., Tollerud, E. J., et al. 2013, A&A, 558, A33
Beltrán, M. T., Sánchez-Monge, Á., Cesaroni, R., et al. 2014, A&A, 571, A52
Estalella, R., Anglada, G., Díaz-Rodríguez, A. K., & Mayen-Gijon, J. M. 2019, A&A, 626, A84
Garay, G., & Lizano, S. 1999, PASP, 111, 1049
Gordon, M. A., & Sorochenko, R. L. 2002, Radio Recombination Lines. Their Physics and Astronomical Applications, Vol. 282 (Dordrecht: Kluwer)
Guzmán, A. E., Garay, G., Brooks, K. J., & Voronkov, M. A. 2012, ApJ, 753, 51
Guzmán, A. E., Garay, G., Rodríguez, L. F., et al. 2014, ApJ, 796, 117
Guzmán, A. E., Sanhueza, P., Zapata, L., Garay, G., & Rodríguez, L. F. 2020, ApJ, 904, 77
Hosokawa, T., & Omukai, K. 2009, ApJ, 691, 823
Keto, E. 2007, ApJ, 666, 976
Keto, E., & Wood, K. 2006, ApJ, 637, 850
Kuiper, R., Klahr, H., Beuther, H., & Henning, T. 2011, ApJ, 732, 20
Kurtz, S., Cesaroni, R., Churchwell, E., Hofner, P., & Walmsley, C. M. 2000, in Protostars and Planets IV, ed. V. Mannings, A. P. Boss, & S. S. Russell (Tucson, AZ: Univ. of Arizona Press), 299
Kurtz, S. E. 2000, RMxAC, 9, 169
Martín, S., Martín-Pintado, J., Blanco-Sánchez, C., et al. 2019, A&A, 631, A159
Mayen-Gijon, J. M., Anglada, G., Osorio, M., et al. 2014, MNRAS, 437, 3766
McMullin, J. P., Waters, B., Schiebel, D., Young, W., & Golap, K. 2007, in ASP Conf. Ser. 376, Astronomical Data Analysis Software and Systems XVI, ed. R. A. Shaw, F. Hill, & D. J. Bell (San Francisco, CA: ASP), 127
Mehringer, D. M. 1994, ApJS, 91, 713
Mezger, P. G., & Henderson, A. P. 1967, ApJ, 147, 471
Mezger, P. G., Smith, L. F., & Churchwell, E. 1974, A&A, 32, 269
Moisés, A. P., Damineli, A., Figuerêdo, E., et al. 2011, MNRAS, 411, 705
Nakano, T. 1989, ApJ, 345, 464
Narayanan, G., Walker, C. K., & Buckley, H. D. 1998, ApJ, 496, 292
Norberg, P., & Maeder, A. 2000, A&A, 359, 1025
Ossenkopf, V., & Henning, T. 1994, A&A, 291, 943
Panagia, N. 1973, AJ, 78, 929
Sánchez-Monge, Á., Cesaroni, R., & Beltrán, M. T. 2013, A&A, 552, L10
Scoville, N. Z., & Kwan, J. 1976, ApJ, 206, 718
Tan, J. C., Beltrán, M. T., Caselli, P., et al. 2014, in Protostars and Planets VI, ed. H. Beuther et al. (Tucson, AZ: Univ. of Arizona Press), 149
Urquhart, J. S., Busfield, A. L., Hoare, M. G., et al. 2007, A&A, 474, 891
Zapata, L. A., Palau, A., Galván-Madrid, R., et al. 2015, MNRAS, 447, 1826
Zhang, Y., Tan, J. C., & Hosokawa, T. 2014, ApJ, 788, 166